


Gyrotropy-governed isofrequency surfaces and photonic spin in gyromagnetic mediaRajarshi Sen  and Sarang Pendharker **Department of Electronics and Electrical Communication Engineering,
Indian Institute of Technology Kharagpur, Kharagpur, West Bengal, India* (Received 27 January 2021; accepted 7 February 2022; published 25 February 2022)

In this paper, we investigate the effect of gyromagnetic terms on the topology of isofrequency surfaces. The diagonal terms of the permeability tensor are known to govern the topology of isofrequency surfaces. However, here we show that the off-diagonal gyrotropic terms of the material tensor also govern the existence of isofrequency surfaces. The relative strength of the gyrotropic term with respect to the permeability term decides the number of isofrequency surfaces which can exist in a gyromagnetic medium. We show that gyrotropy can either suppress an isofrequency surface or support an otherwise nonexistent isofrequency surface. Moreover, the dependence of isofrequency surfaces on gyrotropy is linked to the photonic spin of these isofrequency surfaces. Further, the photonic-spin profile indicates that the photonic spin is locked to the material and not the direction of momentum. This leads to a conflict between spin-momentum locking and material-locked photonic spin, which can be exploited in waveguiding structures to get an asymmetric mode profile and gyrotropy-induced cutoff.

DOI: [10.1103/PhysRevA.105.023528](https://doi.org/10.1103/PhysRevA.105.023528)**I. INTRODUCTION**

Gyrotropic materials are the most commonly employed materials for achieving nonreciprocity in wave propagation from optical to microwave frequencies. Gyroelectric properties have been used to achieve nonreciprocal wave propagation [1–4], isolation [5], asymmetric, and extreme scattering properties in plasmonic structures [6,7] at optical frequencies. Traditionally, gyromagnetic materials have been extensively used in nonreciprocal devices at microwave frequencies [8–10], with microwave isolators and circulators being their primary applications. Conventionally, such gyromagnetic devices were bulky and not suitable for system integration. However, recently researchers have successfully integrated ferrite slabs in substrate-integrated waveguides [11] for nonreciprocal mode conversion and for filter applications [12]. The application of ferrite nanoconduits for nanometer-scale RF magnonic interconnects has also been reported recently [13]. Even though gyromagnetic materials have been employed in microwave applications for decades, the investigation and control of the supported wave characteristics still form an active area of research. In Refs. [14,15], hyperbolic isofrequency surfaces were reported for bulk propagation. In Refs. [16,17], negative refraction and a tunable focusing effect in a gyromagnetic medium were attributed to the hyperbolic dispersion in the gyromagnetic medium. Experimental demonstration of the hyperbolic nature of bulk isofrequency surfaces was demonstrated in Ref. [18]. The hyperbolic nature of isofrequency surfaces in gyromagnetic materials arises due to negative permeability along two directions of the material.

The topology of the isofrequency surfaces is primarily governed by the anisotropic permittivity and permeability of

the material, which can be tailored by forming a composite substrate from layered materials [19–22]. Wide applications of engineered materials exhibiting hyperbolic isofrequency curves [23–27] have been reported in the past. Prominent applications of hyperbolic materials include superresolution microscopy with hyperlensing [28,29], enhanced near-field thermal radiation [30], and thresholdless Cherenkov radiation [31–33].

Combining engineered hyperbolic dielectric properties with gyromagnetic material [34,35] provides integration of engineered isofrequency surfaces with gyrotropic properties. Reference [34] presents the behavior of surface magnon polaritons governed by the hyperbolic topology in a canted antiferromagnetic crystal. More recently, photonic Chern insulators using gyromagnetic hyperbolic metamaterial formed by a superlattice of indium-antimony and yttrium iron garnet [35] has been reported. In Ref. [36], the effect of negative effective permeability on the bihyperbolic nature of isofrequency surfaces has been investigated. However, the specific effect of the gyrotropic terms (off-diagonal terms in the permeability tensor) on the isofrequency surfaces and the mechanism by which gyrotropy affects the isofrequency surfaces requires a comprehensive investigation.

In this paper, we extensively investigate the effect of gyrotropy on the isofrequency surfaces. We report the gyrotropy-imposed conditions on the existence of isofrequency surfaces and reveal that the effect of gyrotropy is intricately linked with the photonic spin of the electromagnetic (EM) waves in the medium. The photonic spin of EM waves has attracted interest in recent years [37–41]. The presence of photonic spin has been reported in surface polaritons [42], spin-momentum locking in reciprocal structures [43–45], spin-governed optical forces [46–48], and spin-photonic forces in nonreciprocal waveguides [49]. Here we report that the photonic spin also plays a central role in controlling the existence and shape of

*sarang@ece.iitkgp.ac.in

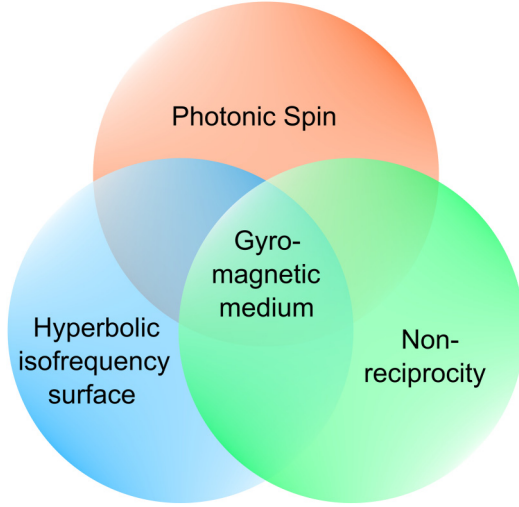


FIG. 1. Gyromagnetic materials exhibit the three important yet seemingly different phenomena of photonic spin, nonreciprocity, and hyperbolic isofrequency surface.

isofrequency surfaces in a gyromagnetic medium. Here, we report the nature of photonic spin along the three-dimensional (3D) isofrequency surfaces for a gyromagnetic medium in elliptical and hyperbolic regimes. We show that when the gyrotropy is strong, it can suppress the existence of one of the isofrequency surfaces, which would have existed in a nongyromagnetic medium. Similarly, a strong gyrotropy can support the existence of an isofrequency surface that would not exist in the absence of gyrotropy. Further, we show that the spin profile along an isofrequency surface is locked to the direction of magnetic bias and not to the direction of propagation, resulting in a violation of spin-momentum locking. We also consider a case where interaction between structure-induced and material-induced photonic spin leads to an asymmetric mode profile in a waveguide. Moreover, we report that the dominance of material-induced spin over structure-induced spin leads to a gyrotropy-controlled cutoff condition for the waveguide. The analysis presented in this paper shows that photonic-spin also plays a crucial role in the propagation characteristics in a gyromagnetic medium. Thus, gyromagnetic materials exhibit the three important electromagnetics wave phenomena, namely, (i) hyperbolic isofrequency surfaces, (ii) photonic spin, and (iii) nonreciprocity, as illustrated in Fig. 1. The analysis presented in this paper will provide guiding principles for engineering gyrotropy of materials for controlling the isofrequency surfaces and the photonic-spin profile.

The paper is organized as follows. In Sec. II, we report that the relative magnitude of the permeability and gyrotropy terms either suppresses or supports the existence of isofrequency surfaces. In Sec. III, the photonic-spin profile of isofrequency surfaces in elliptical and hyperbolic regimes is investigated. It is shown that the photonic spin is locked to the material, and when the gyrotropy is strong, the photonic spin only along the direction of magnetic bias is supported. In Sec. IV, we show that the material-locked nature of photonic spin in gyromagnetic material comes in conflict with

the structure-induced transverse photonic spin in guided-wave structures and leads to an asymmetric mode profile and gyrotropy-induced cutoff.

II. GYROTROPY-CONTROLLED ISOFREQUENCY SURFACES

In this section, we investigate the effect of gyromagnetic terms on the topology of the isofrequency surfaces in a general gyromagnetic medium, with permeability tensor $\vec{\mu}_r$, given by [8]

$$\vec{\mu}_r = \begin{bmatrix} \mu' & -j\kappa' & 0 \\ j\kappa' & \mu' & 0 \\ 0 & 0 & 1 \end{bmatrix}. \quad (1)$$

We consider a magnetic medium biased in the \hat{z} direction. Here, μ' is the permeability term along \hat{x} and \hat{y} directions, and κ' represents gyrotropy. The equation governing the topology of isofrequency surfaces of the medium is (see Appendix A)

$$0.5\epsilon_r k_0^2 (k_r^4 (\mu' + 1) + 2\epsilon_r^2 k_0^4 (\mu'^2 - \kappa'^2) + \epsilon_r k_0^2 k_r^2 (\kappa'^2 - \mu' (3 + \mu'))) - k_r^2 (k_r^2 (\mu' - 1) + \epsilon_r k_0^2 (\kappa'^2 + \mu' - \mu'^2)) \cos 2\theta = 0. \quad (2)$$

Here, the dielectric permittivity of the medium is denoted by ϵ_r . k_0 is the propagation constant in free space. The term k_r defines the propagation constant in the medium over spherical coordinates. θ represents the angle of elevation. Isofrequency surfaces are computed by solving this equation for k_r , which gives two distinct equations due to its biquadratic nature. The two isofrequency surfaces correspond to two different modes. However, depending on the values of μ' and κ' , only one of the surfaces may exist. The effect of the gyrotropic term on the isofrequency surfaces can be understood by taking the following four cases:

- (1) $\mu' > 0$ and $|\mu'| > |\kappa'|$.
- (2) $\mu' > 0$ and $|\mu'| < |\kappa'|$.
- (3) $\mu' < 0$ and $|\mu'| > |\kappa'|$.
- (4) $\mu' < 0$ and $|\mu'| < |\kappa'|$.

Cases (a) and (b) with $\mu' > 0$ support elliptical isofrequency surface, while cases (c) and (d) correspond to the hyperbolic regime. Cases (a) and (c) hold the condition $|\mu'| > |\kappa'|$, whereas, cases (b) and (d) satisfy $|\mu'| < |\kappa'|$. The topology of isofrequency surfaces corresponding to these cases is shown in Fig. 2.

For a positive value of μ' , in a nongyromagnetic ($\kappa' = 0$) medium, we would expect the existence of two concentric ellipsoidal surfaces, touching one another. However, in the presence of gyrotropy ($\kappa' \neq 0$) with the magnitude of the gyrotropic term less than the permeability term, i.e., $|\mu'| > |\kappa'|$, the topology consists of two completely noncontact, concentric ellipsoids as observed in Fig. 2(a). As we increase the magnitude of κ' , the effects of gyrotropy start playing a more prominent role, and when $|\kappa'| > |\mu'|$ only one ellipsoidal isofrequency surface exists, as plotted in Fig. 2(b). Gyrotropy, in this case, limits the topology of the medium to a single isofrequency surface.

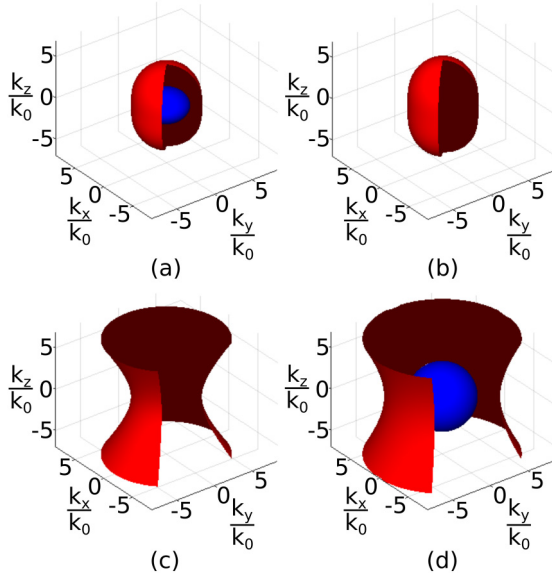


FIG. 2. The topology of isofrequency surfaces in a gyromagnetic medium. (a), (b) The elliptical regime having material parameters (μ', κ') as $(1, 0.75)$ and $(1, 1.25)$, respectively. Free-space propagation constant k_0 corresponds to the frequency of 6 GHz. (c), (d) The hyperbolic regime having material parameters (μ', κ') as $(-1.5, -0.5)$ and $(-1.5, -2.5)$, respectively. k_0 corresponds to the frequency of 11 GHz. (a) It can be seen that for positive μ' two propagating modes exist with ellipsoidal topology when $\mu' > \kappa'$. (b) When $\mu' < \kappa'$ only one ellipsoidal surface exists. (c) For negative μ' , only the hyperbolic mode exists when $|\mu'| > |\kappa'|$. (d) For negative μ' , an additional ellipsoidal isofrequency surface exists when $|\mu'| < |\kappa'|$. The dielectric constant of the medium ϵ_r is 14.

Similarly, when μ' is negative in a nongyromagnetic medium ($\kappa' = 0$), there would exist a single type-II hyperboloid. The negative diagonal terms in the permeability tensor would suppress the existence of the second surface. In the presence of gyrotropy, as long as $|\mu'| > |\kappa'|$, there exists a single hyperbolic isofrequency surface as in Fig. 2(c). However, when $|\mu'| < |\kappa'|$, we get two isofrequency surfaces, one hyperboloid and the second ellipsoid, shown in Fig. 2(d). In this case, the gyrotropy supports the existence of the second ellipsoidal surface, which would otherwise be nonexistent. These conditions are summarized in Table I. Note that, although some of these gyrotropy conditions are achieved in a natural gyromagnetic medium, an engineered gyromagnetic medium may be required to realize some of these cases. In a nutshell, ellipsoidal and hyperbolic isofrequency regimes are the two main classes of isofrequency surfaces depending on the sign of μ' . However, based on the gyrotropicity, a second ellipsoidal isofrequency surface exists in the ellipsoidal

regime when $|\kappa'| < |\mu'|$, and in the hyperbolic regime when $|\kappa'| > |\mu'|$.

While the nature of the isofrequency surface depends on the permeability term, gyrotropy also strongly influences the topology. This influence is manifested in the form of material-induced photonic spin, along the isofrequency surfaces, and forms the subject of investigation in Sec. III.

III. PHOTONIC SPIN PROFILE OF ISOFREQUENCY SURFACES

The sense of rotation of fields in electromagnetic waves has been characterized as photonic spin [37–41]. Note that this photonic spin is different from conventional magnon polaritons, where the later deals with coupling of EM energy with the magnetic dipoles of the medium. The net photonic spin of a medium is defined as the combination of both electric ($\text{Im}\{\vec{E}^* \times \vec{E}\}$) and magnetic ($\text{Im}\{\vec{H}^* \times \vec{H}\}$) photonic spins. Since we are considering a gyromagnetic medium, we are concerned with the photonic spin of a magnetic field defined by $\vec{S} = \text{Im}\{\vec{H}^* \times \vec{H}\}$. This definition of spin is equivalent to defining the three-dimensional third Stokes parameter for the magnetic field (see Appendix C). In this section, we investigate the photonic-spin profile of the isofrequency surfaces and reveal the photonic-spin-dependent nature of gyrotropy-imposed conditions on the topology, which were reported in the previous section. We consider a gyromagnetic material biased in the \hat{z} direction. To compute the photonic spin of \vec{H} , the magnetic vector components H_y and H_z are expressed relative to H_x , using the condition $[\vec{k} \cdot \vec{k} + k_0^2 \epsilon_r \mu_r] \cdot \vec{H} = 0$. To plot the spin profile of the isofrequency surfaces, the fields are converted from Cartesian (H_x, H_y, H_z) to spherical (H_r, H_θ, H_ϕ) , and normalized to limit the Stokes parameter value within the range of -1 to 1 . The three components of the spin are then computed in the spherical coordinates as $\vec{S} = S_r \hat{r} + S_\theta \hat{\theta} + S_\phi \hat{\phi}$, where each of these orthogonal spin components can be individually explored.

Figure 3 maps the photonic spin of the magnetic field along the isofrequency surfaces, corresponding to the ellipsoidal and hyperbolic regimes. We can observe from Table I that, depending on the material parameters μ' and κ' , either one or two isofrequency surfaces will exist. To present a comprehensive mapping of the spin profile, we select the values of μ' and κ' following Table I, such that two isofrequency surfaces exist for both the elliptical and hyperbolic regimes. Figure 3(a) shows the radial (longitudinal) spin S_r when $\mu' > 0$ and $|\mu'| > |\kappa'|$, while Fig. 3(b) shows S_r when $\mu' < 0$ and $|\mu'| < |\kappa'|$. These two cases correspond to the ellipsoidal and hyperbolic regimes, respectively. From Fig. 3(a), it can be seen that S_r reaches its extreme values along the positive and negative z axis (the axis of bias), with the two isofrequency

TABLE I. Topological regimes for different values of μ' and κ' , as depicted in Fig. 2.

Gyrotropic term	$\mu' > 0$ (Ellipsoidal regime)	$\mu' < 0$ (Hyperbolic regime)
$\kappa' = 0$	Two concentric touching ellipsoids	Single hyperboloid
$ \mu' > \kappa' $	Two concentric nontouching ellipsoids	Single hyperboloid
$ \mu' < \kappa' $	A single ellipsoid	One hyperboloid and one ellipsoid

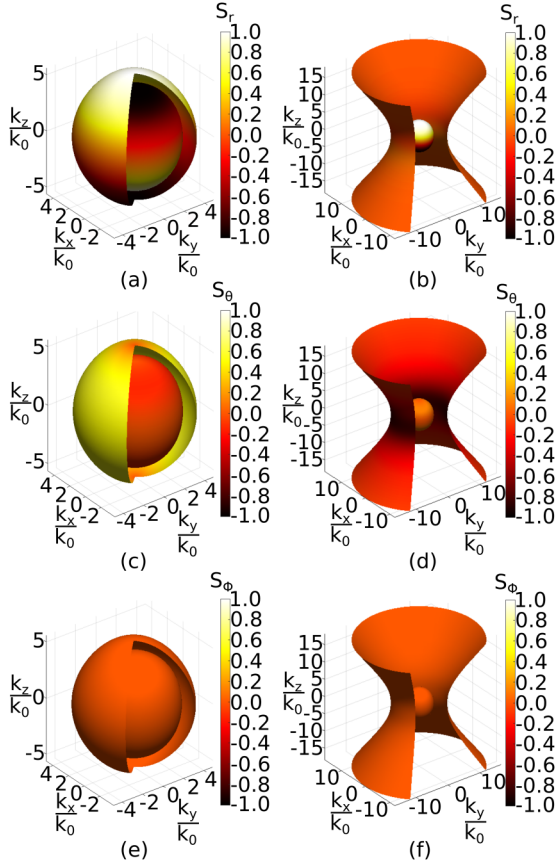


FIG. 3. Representation of photonic-spin profile on the isofrequency surfaces corresponding to ellipsoidal and hyperbolic regimes. Material parameters μ' and κ' are selected to allow the existence of two isofrequency surfaces. Material parameters (μ' , κ') are (a), (c), (e) (1.79, 0.47) and (b), (d), (f) (−1.38, 2.62), respectively. The free-space propagation constant k_0 for ellipsoidal and hyperbolic regimes corresponds to the frequencies of 6 and 11 GHz, respectively. Spin profiles along the (a), (b) \hat{r} direction, (c), (d) $\hat{\theta}$ direction, and (e), (f) $\hat{\phi}$ direction, respectively.

surfaces supporting opposite spins. In the hyperbolic regime, Fig. 3(b), it can be seen that one surface is hyperbolic with S_r having significantly low magnitude. Figures 3(c) and 3(d) represent S_θ , and Figs. 3(e) and 3(f) show the spin S_ϕ component in the two regimes, respectively. It is also observed from Figs. 3(e) and 3(f) that no spin exists for the S_ϕ for both the regimes. Since there is an axial symmetry around the direction of bias— \hat{z} in this case—we can limit our analysis to the k_x - k_z plane without loss of generality.

To further investigate the interlink between photonic spin and the gyrotropy-imposed conditions over the two topological regimes, we compute the photonic spin along the isofrequency surfaces while restricting the wave propagation along the x - z plane.

A. Elliptical regime

We first analyze the spin profile along the isofrequency curves in the k_x - k_z plane in the elliptical regime. For in-plane propagation, the y and z components of the magnetic field can be expressed in terms of H_x in the form of analytical

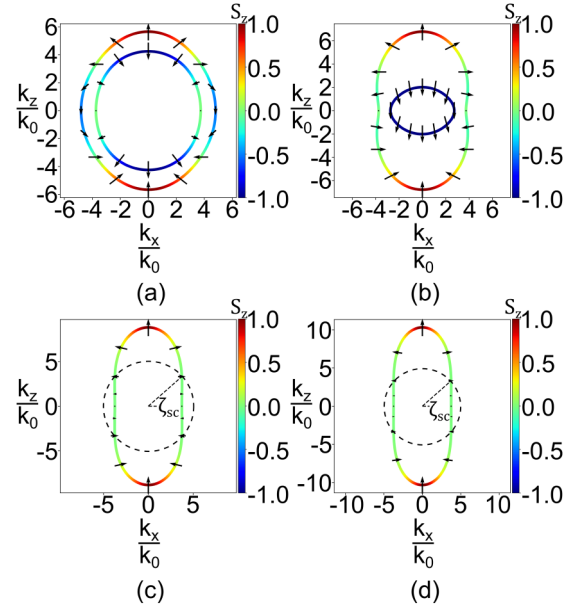


FIG. 4. Representation of photonic-spin profile along the two-dimensional (2D) isofrequency contours for the elliptical regime. Color map shows the \hat{z} -oriented spin (S_z). The arrows represent the direction and magnitude of the spin. Free-space propagation constant k_0 corresponds to the frequency of 6 GHz. μ' is fixed at 1.79, whereas panels (a)–(d) correspond to the values of κ' as 0.5, 1.5, 3.8, and 5.8, respectively.

expressions (see Appendix B), given by

$$H_y = -\frac{j\epsilon_r k_0^2 \kappa'}{\epsilon_r k_0^2 \mu' - k_r^2} H_x \quad (3)$$

and

$$H_z = -\frac{k_r^2 \cos \theta \sin \theta}{\epsilon_r k_0^2 - k_r^2 \sin^2 \theta} H_x. \quad (4)$$

From Eqs. (3) and (4), it can be seen that x and z components of the magnetic field are in phase while the y component is 90° out of phase. Note that κ' appears in the numerator of Eq. (3) as a linear term, indicating the presence of a gyrotropy-induced spin in the EM wave, which reverses its direction with the sign of κ' .

Photonic spins for the elliptical regime are computed for a fixed permeability value $\mu' = 1.79$ while varying the value of κ' from 0.5 to 5.8. The resultant spin profiles along the isofrequency surfaces are shown in Fig. 4. The arrows represent the magnitude and direction of net spin, and the color map of the contour represents the spin S_z , i.e., the spin component along the direction of the magnetic bias. The values of κ' are selected such that Figs. 4(a) and 4(b) correspond to the case when $|\mu'| > |\kappa'|$ and two isofrequency surfaces are supported. The gyrotropic effect, in this case, allows the existence of both modes. The inner isofrequency contour holds a negative spin along the \hat{z} axis; i.e., the spins are antiparallel to the direction of bias for this mode. For the outer isofrequency surface, though, both parallel as well as antiparallel spins exist. As the gyrotropy increases further, the spins over the inner ellipse align further antiparallel, and the ellipse shrinks. When $|\mu'| < |\kappa'|$ the inner ellipse ceases to exist. Figures 4(c)

and 4(d) depict this condition. In this scenario, the gyrotropy is strong enough to suppress the inner ellipse, which had photonic spin antiparallel to the magnetic bias.

We observe an additional effect of the gyrotropy over the outer ellipsoid of Fig. 4. The photonic spin corresponding to the inner ellipsoid along the z axis is entirely negative. In comparison, the outer ellipse contains both positive and negative photonic spin along the z axis. There is a specific spin-crossover angle ζ_{sc} (with respect to the \hat{x} axis) over the isofrequency surface, below and above which the photonic spins along the z axis are observed to be negative and positive, respectively. As we increase the value of κ' , the photonic spin below ζ_{sc} having negative spin sense along the z axis tends to diminish. Note that though we only show ζ_{sc} in Figs. 4(c) and 4(d) for the sake of simplicity; this crossover angle exists for the entire elliptical regime. This crossover angle ζ_{sc} is given by (see Appendix D)

$$\zeta_{sc} = \cos^{-1} \sqrt{\frac{1}{\mu'}}. \quad (5)$$

Interestingly, Eq. (5) is independent of the gyrotropic term κ' . The definition of ζ_{sc} using Eq. (5) is only valid for the elliptical regime (positive μ'), whereas it is invalid for the hyperbolic regime (negative μ'). The spin-crossover angle ζ_{sc} can be physically interpreted as the intersection of the isofrequency curve with the circle [see the dashed circle in Figs. 4(c) and 4(d)] defined as $k_x^2 + k_z^2 = k_0^2 \sqrt{\mu' \epsilon_r}$.

In addition to the inner ellipse being suppressed once gyrotropy is strong enough, we can observe the antiparallel spins below ζ_{sc} being diminished, making the region increasingly spinless. Moreover, parallel photonic spins lead to elongation of the outer ellipse along the bias direction with an increasing gyrotropy.

B. Hyperbolic regime with gyrotropy-supported secondary isofrequency surface

Similar to Sec. III A, we investigate the photonic-spin profile in the hyperbolic regime over the isofrequency surfaces by taking a fixed value of $\mu' = -1.38$, and four distinct values of κ' . Isofrequency contours corresponding to the κ' values of 0.5 and 1.1, are shown in Figs. 5(a) and 5(b), respectively. These values satisfy the condition of $|\mu'| > |\kappa'|$, where the gyrotropy is not strong enough to support the elliptical mode, and only the hyperbolic mode exists. For smaller values of $|\kappa'|$, the photonic spin along the hyperbolic isofrequency curve is negligibly weak. The hyperbolic mode, in this case, is predominantly spinless. The other two values, $\kappa' = 2.5$ and 5, hold the condition $|\mu'| < |\kappa'|$, where the gyrotropy can support the existence of the second elliptical mode. These two cases are shown in Figs. 5(c) and 5(d), respectively. Note that the spins along the elliptical isofrequency contour are aligned parallel to the direction of bias. Thus a strong gyrotropy can support an isofrequency surface, which otherwise would not have existed in a nongyromagnetic or a weakly gyromagnetic medium.

The hyperbolic mode also shows interesting spin characteristics. Increasing the magnitude of $|\kappa'|$ makes the spins along the hyperbolic isofrequency curve more prominent. However,

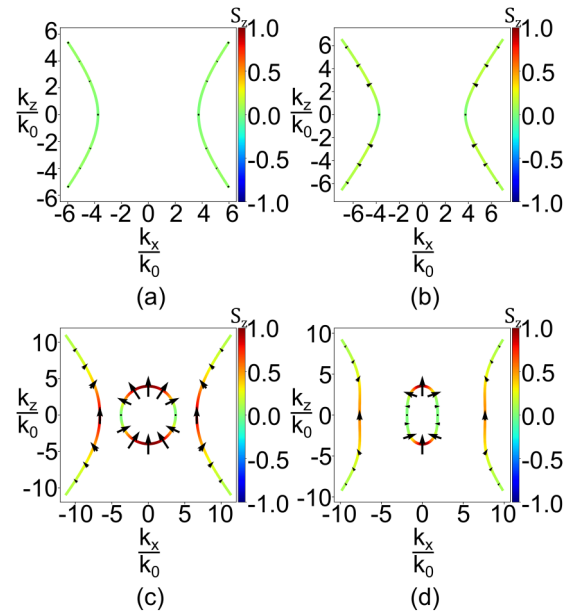


FIG. 5. Representation of photonic-spin profile along the 2D isofrequency contours for the hyperbolic regime. Color map shows the \hat{z} -oriented spin (S_z). The arrows represent the direction and magnitude of the spin. Free-space propagation constant k_0 corresponds to the frequency of 11 GHz. μ' is fixed at -1.38 , whereas panels (a)–(d) correspond to the values of κ' as 0.5, 1.1, 2.5, and 5, respectively.

the hyperbolic mode has significantly low longitudinal (radial) spin throughout the curve, and the net spin also goes to zero along the asymptote of the hyperbola. Near the k_x axis, the spin is aligned parallel to the direction of bias.

Thus gyrotropic terms play an important role in influencing the existence and shape of the isofrequency surfaces, and hence the wave propagation characteristics in a gyromagnetic medium. This influence is mediated via the photonic spin. Therefore, engineering the gyrotropicity of the medium can lead to interesting device-level applications, especially where photonic spin is also involved. In the next section, we show that the material-locked nature of the photonic spin in a gyromagnetic medium leads to an asymmetric mode profile and a gyrotropy-induced cutoff in a guided-wave structure.

IV. MATERIAL-LOCKED PHOTONIC SPIN IN GUIDED-WAVE STRUCTURE

The photonic-spin profile of the isofrequency surfaces investigated in the previous section reveals that the spins for a pair of antipodal points on the isofrequency surfaces are aligned in the same direction. This indicates that even the transverse photonic spin for two counterpropagating waves is aligned in the same direction and does not revert with the direction of propagation. However, it has been reported that the photonic spin is locked to the direction of propagation [43]. The nonreversal of spin with the reversal of direction of propagation indicates the disruption of this spin-momentum locking in a gyromagnetic medium. In this section, we discuss the potential application of the breaking of spin-momentum locking in waveguiding structures filled with gyromagnetic material.

A. Spin-momentum locking in a waveguide

In Ref. [43], Van Mechelen and Jacob reported that the transverse spin is locked to the direction of propagation and that this locking is a universal phenomenon. In Ref. [46], Kalhor *et al.* showed that the locking of transverse spin to the direction of propagation is responsible for the direction-dependent transverse optical forces on chiral particles. Spin-momentum locking in the near field of metal nanostructures was reported in Ref. [50]. In Ref. [49], Pendharker *et al.* showed that the photonic spins of two counterpropagating waves are opposite but not equal (nondegenerate) as the time reversal is broken by motion-induced nonreciprocity.

The reversal of photonic spin with the direction of propagation is also observed across the cross section of typical waveguiding structures. The analytical equation defining the photonic spin for a dielectric-filled parallel plate waveguide (y is taken from $-a/2$ to $a/2$) in its dominant mode is given as

$$\bar{S}_{z,\text{diel}} = \sin\left(2 \tan^{-1}\left(\frac{ak_x}{\pi} \cot\left(\frac{\pi y}{a}\right)\right)\right). \quad (6)$$

This equation indicates symmetrical photonic spin reversal for forward- and backward-propagating waves, which will have the k_x of the same magnitude but positive and negative signs, respectively.

Let us consider a transverse electric (TE) mode of propagation in a simple metallic rectangular waveguide filled with nongyrotropic material as shown in Fig. 6(a). The magnetic field of the propagating mode has out-of-phase longitudinal and transverse components, which results in a transverse photonic spin. We call this the structure-induced spin because it arises from the bounded nature of wave propagation. This photonic spin $\bar{S} = \text{Im}\{\bar{H}^* \times \bar{H}\}$ computed over the values obtained through CST Microwave Studio simulation is shown for the forward and backward propagation in Figs. 6(b) and 6(c), respectively. It can be observed that the spin profile is symmetric about the center ($y = 0$), and with the reversal of the direction of propagation, the sign of the spin profile also reverses.

B. Material-induced spin versus spin-momentum locking

We have seen in Sec. III that gyrotropic medium exhibits material-induced spin where the two counterpropagating modes have equal and aligned spins. On the other hand, the structure-induced spin reverts its direction for counterpropagating modes. In a scenario where both these spins are oriented along the same axis, we would expect the material-induced spin to maintain its direction on the reversal of propagation. On the contrary, the structure-induced spin would tend to reverse its direction due to spin-momentum locking. This happens in a waveguide filled with a gyromagnetic medium which is also biased in the direction of the structure-induced spin.

Let us consider a rectangular waveguide with dimensions similar to that of the dielectric waveguide of Sec. IV A [see Fig. 7(a)], but filled with gyromagnetic material and biased along the $+\hat{z}$ direction. The material parameters μ' and κ' are 1.99 and 0.69, respectively. The dielectric permittivity is $\epsilon_r = 14$. k_0 corresponds to the frequency of 7 GHz. This structure

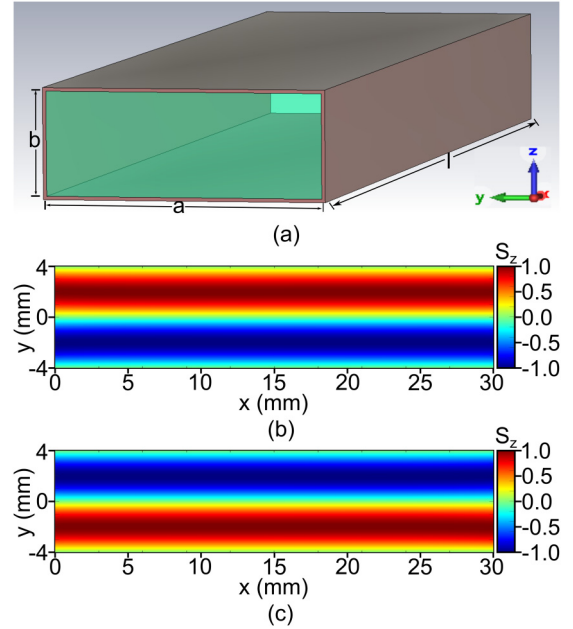


FIG. 6. (a) 3D view of the rectangular waveguide to be simulated. Photonic spin profile of \bar{H} generated using CST simulation for a dielectric-filled rectangular waveguide, corresponding to (b) forward propagation and (c) backward propagation. Conservation of spin-momentum locking is visible. The broader and thinner widths of the waveguide are 8 and 3 mm, along \hat{y} and \hat{z} axes, respectively. Relative permittivity of the dielectric is $\epsilon_r = 14$, and k_0 corresponds to the frequency of 7 GHz. Perfect electric conductor (PEC) boundary conditions are enforced. CST simulations are performed considering the basis function of $e^{j(k_x x - \omega t)}$.

is simulated using CST Microwave Studio to investigate the photonic-spin profile over the cross section of the waveguide for both forward and backward propagation. The EM wave propagation follows a TE_{10} mode. Figures 7(b) and 7(c) show the photonic-spin profile for \bar{H} corresponding to forward and backward wave propagation, respectively. As opposed to the symmetric spin profile of structure-induced spin, where the positive and negative spins exist in equal proportions, here, the region of negative spin exceeds that of the positive spin. This is in agreement with the observed material-induced spin for propagation along the x - y plane. Compared to the spin of the dielectric-filled waveguide, there is a relative expansion of the negative-spin region and shrinkage of the positive-spin region over the cross section. Moreover, the zero-spin region is offset from the center, which asserts the asymmetry of the spin profile. In addition, the negative spin dominates for both the forward and backward propagation, indicating the presence of material-induced spin. This asymmetric mode profile can have several applications in nonreciprocal waveguiding structures. For instance nonreciprocal mode conversion was reported in Ref. [11]. However, the photonic-spin origin of the nonreciprocity in the mode profile was not pointed out there.

C. Gyrotropy-induced cutoff

To get a better physical understanding of this interaction between material-induced spin and structure-induced spin, we analytically explore a parallel plate waveguide filled with

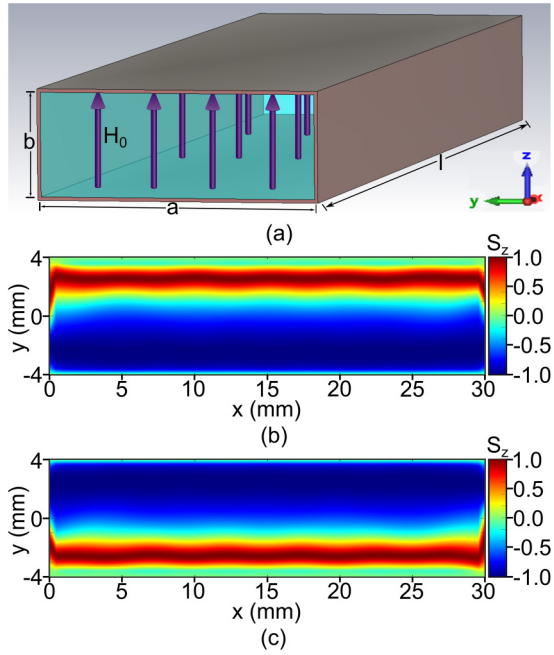


FIG. 7. CST Microwave Studio simulation results, comparison of the spin-profile nonreciprocity for forward- and backward-propagating wave, comparing dielectric filled ($\epsilon_r = 14$) and gyrotropic material filled (\hat{z} biased with $\epsilon_r = 14$, $\mu' = 1.99$, and $\kappa' = 0.69$) rectangular waveguide. Free-space propagation constant k_0 corresponds to the frequency of 7 GHz. Spin profile is represented for the X - Y plane at $z = 0$. (a) 3D view of the waveguide, $l = 30$ mm, $a = 8$ mm, and $b = 3$ mm. Uniform magnetic bias H_0 is represented as purple arrows along $+\hat{z}$. Magnetic field spin profile for gyrotropic material filled waveguide with (b) forward and (c) backward propagation, respectively. CST simulations are performed considering the basis function of $e^{j(k_x x - \omega t)}$.

gyromagnetic material. The parallel plate waveguide has an infinite extension along the \hat{z} direction, enabling a 2D analysis in the x - y plane. The side view of the waveguide is shown in Fig. 8(a). The gyromagnetic medium is biased along $+\hat{z}$, which is aligned along the direction of structure-induced spin. The plate separation is 6 mm, and PEC boundary conditions are enforced.

The spin profile corresponding to the forward propagation along the waveguide is shown in Fig. 8(b). The asymmetrical spin profile is visible. Negative spin dominates the overall photonic-spin profile. Gyromagnetic medium parameters are $\mu' = 1.99$ and $\kappa' = 0.69$. Our analytical approach highlights spin asymmetry and nonreciprocity more prominently.

As we increase the gyrotropic term κ' , the material-induced negative spin dominates, and the positive spin diminishes. This is shown in Fig. 8(c) for the forward-propagating mode. When $\kappa' = 0$, the spin profile is symmetric. However, as the magnitude of κ' increases, the spin profile starts becoming more asymmetric, with a greater region of the cross section trying to align with the material-induced spin. The structure-induced spin, however, tries to maintain the positive and negative spin profile across the cross section. Once the positive spin ceases to exist, it triggers a cutoff condition in wave propagation. We call this the gyrotropy-induced cutoff.

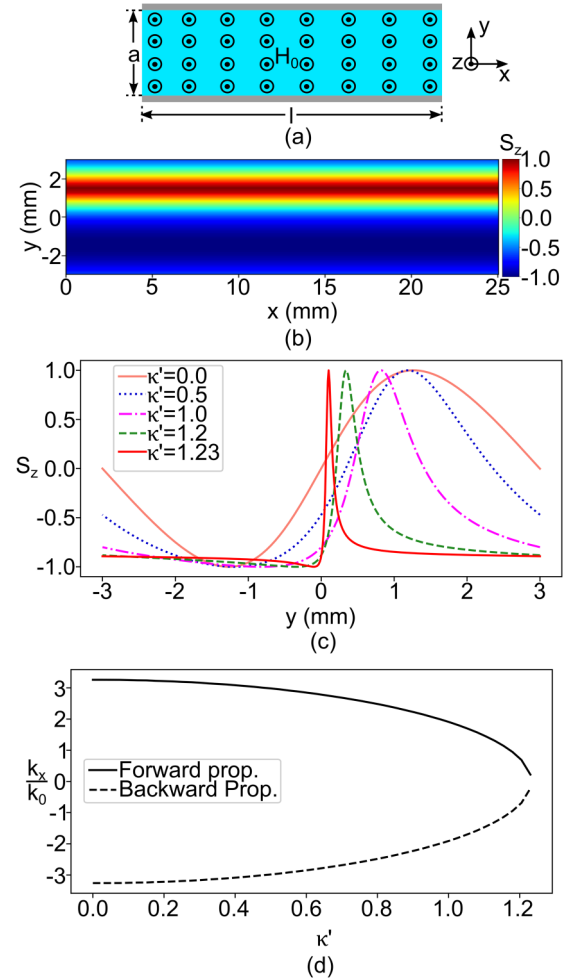


FIG. 8. (a) Side view of the parallel plate waveguide filled with gyrotropic material. Magnetic bias is along $+\hat{z}$. (b) \hat{S}_z spin as a color map for forward propagation. Plate separation distance $a = 6$ mm, $\mu' = 1.99$, and $\kappa' = 0.69$. k_0 corresponds to the frequency of 7 GHz. The spin tries to align mostly along the direction of material-induced spin, resulting in an asymmetric mode profile. (c) Asymmetry of the spin profile S_z along the cross section for varying κ' . (d) The gyrotropy-induced cutoff as a result of increased κ' .

Figure 8(d) shows the diminishing of the propagation constant k_x with the increasing dominance of material-induced spin. As we increase the magnitude of κ' , the suppression results in a gyrotropy-induced cutoff, where k_x goes to zero.

V. CONCLUSION

In this paper, we have investigated the photonic-spin profile in a general gyromagnetic medium. We have revealed the relationship between the topology of isofrequency surfaces and the underlying photonic-spin profile. We have shown that gyrotropy can completely suppress an isofrequency surface or support an otherwise nonexistent surface. Further, we have shown that the material-induced spin violates spin-momentum locking, which results in a conflict with the structure-induced spin in a waveguiding structure. Due to this conflict, an asymmetric mode profile and a gyrotropy-induced cutoff are observed in guided-wave structures. Engineering gyrotropy,

along with permeability and permittivity, can provide an additional degree of freedom for designing engineered materials. Further, since the external biasing field can tune gyrotropy, the results presented in this paper may lead to a new class of gyrotropy-controlled tunable components.

APPENDIX A: DERIVATION OF 3D ISOFREQUENCY SURFACE AND FIELD EQUATIONS

Wave propagation in a medium can be understood with the help of its propagation constant k along the principal axes.

These principal components of the propagation constant along \hat{x} , \hat{y} , and \hat{z} in the polar form are $k_r \sin \theta \cos \phi$, $k_r \sin \theta \sin \phi$, and $k_r \cos \theta$, respectively. Using these values of k along the principal axes, we find a k -tensor \overleftrightarrow{k} , such that the curl operation for the electric and magnetic field can be replaced with a matrix multiplication with the \overleftrightarrow{k} ; i.e., $\nabla \times \vec{E}$ and $\nabla \times \vec{H}$ is equivalent to $\overleftrightarrow{k} \cdot \vec{E}$ and $\overleftrightarrow{k} \cdot \vec{H}$, respectively. The generalized 3D k -tensor \overleftrightarrow{k} in the polar form is

$$\overleftrightarrow{k} = \begin{bmatrix} 0 & -k_r \cos \theta & k_r \sin \theta \sin \phi \\ k_r \cos \theta & 0 & -k_r \sin \theta \cos \phi \\ -k_r \sin \theta \sin \phi & k_r \sin \theta \cos \phi & 0 \end{bmatrix}. \quad (\text{A1})$$

Using this \overleftrightarrow{k} in the wave equation of the form $\det([\overleftrightarrow{k} \cdot \overleftrightarrow{k} + \epsilon_r k_0^2 \overleftrightarrow{\mu}_r]) = 0$, we get

$$0.5\epsilon_r k_0^2 (k_r^4 (\mu' + 1) + 2\epsilon_r^2 k_0^4 (\mu'^2 - \kappa'^2) + \epsilon_r k_0^2 k_r^2 (\kappa'^2 - \mu' (3 + \mu'))) - k_r^2 (k_r^2 (\mu' - 1) + \epsilon_r k_0^2 (\kappa'^2 + \mu' - \mu'^2)) \cos 2\theta = 0. \quad (\text{A2})$$

Solving Eq. (A2) for the roots gives the solution k_r . We get two independent solutions from this biquadratic equation as the two isofrequency surfaces:

$$k_{r1} = \sqrt{\epsilon_r} k_0 ((\kappa'^2 - 3\mu' - \mu'^2 - \cos 2\theta (\kappa'^2 + \mu' - \mu'^2) + (8(\mu'^2 - \kappa'^2)(-1 - \mu' + (\mu' - 1) \cos 2\theta) + (-\kappa'^2 + \mu'(3 + \mu') + (\kappa'^2 + \mu' - \mu'^2) \cos 2\theta)^2)^{0.5}) / (2(-1 - \mu' + (\mu' - 1) \cos 2\theta)))^{0.5}, \quad (\text{A3})$$

$$k_{r2} = \sqrt{\epsilon_r} k_0 ((\kappa'^2 - 3\mu' - \mu'^2 - \cos 2\theta (\kappa'^2 + \mu' - \mu'^2) - (8(\mu'^2 - \kappa'^2)(-1 - \mu' + (\mu' - 1) \cos 2\theta) + (-\kappa'^2 + \mu'(3 + \mu') + (\kappa'^2 + \mu' - \mu'^2) \cos 2\theta)^2)^{0.5}) / (2(-1 - \mu' + (\mu' - 1) \cos 2\theta)))^{0.5}. \quad (\text{A4})$$

We see that the k_r solutions are independent of the azimuth variable ϕ , which supplements our approach of analyzing the isofrequency surface as its two-dimensional variants as isofrequency contours. Using the wave equation for the elimination of the magnetic field $[\overleftrightarrow{k} \cdot \overleftrightarrow{k} + \epsilon_r k_0^2 \overleftrightarrow{\mu}_r] \cdot \vec{H} = 0$, we find the y and z components of the magnetic field with respect to the x component:

$$H_y = H_x \frac{j\epsilon_r k_0^2 \kappa' \cos \phi + (k_r^2 - \epsilon_r k_0^2 \mu') \sin \phi}{(k_r^2 - \epsilon_r k_0^2 \mu') \cos \phi - j\epsilon_r k_0^2 \kappa' \sin \phi}, \quad (\text{A5})$$

$$H_z = H_x \frac{(k_r^4 - 3\epsilon_r k_0^2 k_r^2 \mu' + 2\epsilon_r^2 k_0^4 (\mu'^2 - \kappa'^2) + k_r^2 (k_r^2 - \epsilon_r k_0^2 \mu') \cos 2\theta) \csc \theta \sec \theta}{2k_r^2 ((k_r^2 - \epsilon_r k_0^2 \mu') \cos \phi - j\epsilon_r k_0^2 \kappa' \sin \phi)}. \quad (\text{A6})$$

Equations (A5) and (A6) give the H_y and H_z components of the magnetic field with respect to H_x , respectively.

APPENDIX B: DERIVATION OF 2D ISOFREQUENCY CURVES AND FIELD EQUATIONS

Apart from the 3D isofrequency surface equations of Appendix A, it is helpful to have dispersion equations for two-dimensional isofrequency curves. This becomes useful when we take advantage of the axial symmetry of 3D isofrequency surfaces.

The \overleftrightarrow{k} defining the wave propagation in the 2D X - Z plane can be defined as

$$\overleftrightarrow{k} = \begin{bmatrix} 0 & -k_r \cos \theta & 0 \\ k_r \cos \theta & 0 & -k_r \sin \theta \cos \phi \\ 0 & k_r \sin \theta \cos \phi & 0 \end{bmatrix}. \quad (\text{B1})$$

Using this \overleftrightarrow{k} in $\det([\overleftrightarrow{k} \cdot \overleftrightarrow{k} + \epsilon_r k_0^2 \overleftrightarrow{\mu}_r]) = 0$, we get

$$\epsilon_r k_0^2 (k_r^4 \cos^4 \theta - (\epsilon_r k_0^2 - k_r^2 \sin^2 \theta \cos^2 \phi) (\epsilon_r k_0^2 (\kappa'^2 - \mu'^2) + k_r^2 \mu' \sin^2 \theta \cos^2 \phi) + \cos^2 \theta (-2\epsilon_r k_0^2 k_r^2 \mu' + k_r^4 (1 + \mu') \sin^2 \theta \cos^2 \phi)) = 0. \quad (\text{B2})$$

We solve Eq. (B2) for k_r to get two independent equations defining the isofrequency curves in the 2D X - Z plane:

$$k_{r1} = \sqrt{\epsilon_r k_0} ((\mu' (2 \cos^2 \theta + \sin^2 \theta \cos^2 \phi) + \sin^2 \theta \cos^2 \phi (\mu'^2 - \kappa'^2) + (4\kappa'^2 \cos^4 \theta + 4\kappa'^2 \sin^2 \theta \cos^2 \theta \cos^2 \phi + (\kappa'^2 + \mu' - \mu'^2)^2 \sin^4 \theta \cos^4 \phi)^{0.5}) / (2(\cos^2 \theta + \sin^2 \theta \cos^2 \phi)(\cos^2 \theta + \mu' \sin^2 \theta \cos^2 \phi)))^{0.5}, \quad (\text{B3})$$

$$k_{r1} = \sqrt{\epsilon_r k_0} ((\mu' (2 \cos^2 \theta + \sin^2 \theta \cos^2 \phi) + \sin^2 \theta \cos^2 \phi (\mu'^2 - \kappa'^2) - (4\kappa'^2 \cos^4 \theta + 4\kappa'^2 \sin^2 \theta \cos^2 \theta \cos^2 \phi + (\kappa'^2 + \mu' - \mu'^2)^2 \sin^4 \theta \cos^4 \phi)^{0.5}) / (2(\cos^2 \theta + \sin^2 \theta \cos^2 \phi)(\cos^2 \theta + \mu' \sin^2 \theta \cos^2 \phi)))^{0.5}. \quad (\text{B4})$$

Using the wave equation for the elimination of the magnetic field $[\vec{k} \cdot \vec{k} + \epsilon_r k_0^2 \vec{\mu}_r] \cdot \vec{H} = 0$, we find the y and z components of the magnetic field with respect to the x component:

$$H_y = H_x \frac{j\epsilon_r k_0^2 \kappa'}{k_r^2 (\cos^2 \theta + \sin^2 \theta \cos^2 \phi) - \epsilon_r k_0^2 \mu'}, \quad (\text{B5})$$

$$H_z = H_x \frac{k_r^2 \sin \theta \cos \theta \cos \phi}{k_r^2 \sin^2 \theta \cos^2 \phi - \epsilon_r k_0^2}. \quad (\text{B6})$$

Equations (B5) and (B6) give H_y and H_z components of \vec{H} with respect to H_x , respectively. Note that, here, the term ϕ takes discrete values of 0° and 180° for forward- and backward-propagating waves, respectively. A simpler form for computation of these field components will be obtained by removing the ϕ term and varying θ from 0° to 360° (with respect to the z axis) instead of the conventional form of 0° to 180° .

APPENDIX C: DEFINITION OF PHOTONIC SPIN FOR MAGNETIC FIELD

The third Stokes parameter S_3 denotes the spin sense and its magnitude in an arbitrary direction. The magnetic field vector \vec{H} in the Cartesian coordinate system can be written in terms of its directional elements as

$$\vec{H} = H_x \hat{x} + H_y \hat{y} + H_z \hat{z}. \quad (\text{C1})$$

Similarly, the conjugate magnetic field vector \vec{H}^* is

$$\vec{H}^* = H_x^* \hat{x} + H_y^* \hat{y} + H_z^* \hat{z}. \quad (\text{C2})$$

The individual directional components of \vec{H} are

$$\begin{aligned} H_x &= |H_x| \exp j\phi_x, \\ H_y &= |H_y| \exp j\phi_y, \\ H_z &= |H_z| \exp j\phi_z. \end{aligned} \quad (\text{C3})$$

We normalize the magnetic field components for simplicity of computation. The cross product of \vec{H}^* and \vec{H} is

$$\begin{aligned} \vec{H}^* \times \vec{H} &= 2j|H_y||H_z| \sin(\phi_z - \phi_y) \hat{x} + 2j|H_z||H_x| \\ &\times \sin(\phi_x - \phi_z) \hat{y} + 2j|H_x||H_y| \sin(\phi_y - \phi_x) \hat{z}. \end{aligned} \quad (\text{C4})$$

The imaginary part of Eq. (C4) is

$$\text{Im}(\vec{H}^* \times \vec{H}) = S_{3x} \hat{x} + S_{3y} \hat{y} + S_{3z} \hat{z}. \quad (\text{C5})$$

The third Stokes parameter S_3 is sufficient to describe the spin profile in any arbitrary direction as a vector sum of spins along the principal axes. The third Stokes parameters for the principal axes are

$$\begin{aligned} S_{3x} &= 2|H_y||H_z| \sin(\phi_z - \phi_y), \\ S_{3y} &= 2|H_z||H_x| \sin(\phi_x - \phi_z), \\ S_{3z} &= 2|H_x||H_y| \sin(\phi_y - \phi_x). \end{aligned} \quad (\text{C6})$$

The third Stokes parameter in Eq. (C6) is normalized to limit S_3 within -1 to 1 .

APPENDIX D: DERIVATION OF THE SPIN-CROSSOVER ANGLE

The spin-crossover angle separates the angular region, defining parallel and antiparallel spin. We use a simplified polar form for defining this spin-crossover angle, which requires the angle measurement to start from the k_x axis and traverse counterclockwise. This leads to a modified \vec{k}_{sc} tensor in the Cartesian form,

$$\vec{k}_{sc} = \begin{bmatrix} 0 & -k_r \sin(\zeta_{sc}) & 0 \\ k_r \sin(\zeta_{sc}) & 0 & -k_r \cos(\zeta_{sc}) \\ 0 & k_r \cos(\zeta_{sc}) & 0 \end{bmatrix}. \quad (\text{D1})$$

Using modified wave equation $[\vec{k}_{sc} \cdot \vec{k}_{sc} + \epsilon_r k_0^2 \vec{\mu}_r] \cdot [\vec{H}] = 0$, the matrix defining the field component relationship is derived. The magnetic field spin in the x - y plane is defined as

$$H_x = -H_y \frac{\epsilon_r k_0^2 \mu' - k_r^2}{j\epsilon_r k_0^2 \kappa'}. \quad (\text{D2})$$

We observe $k_r = k_0 \sqrt{\epsilon_r \mu'}$ leads to zero spin along the bias axis. This point is termed the spin-crossover point as it acts as the boundary separating parallel and antiparallel material-induced spin. Solving the modified wave equation for k_r , we get two expressions representing the two independent isofrequency surfaces. Only one of these isofrequency surfaces demonstrates spin inversion corresponding to the propagation angle. Equating this expression of k_r with $k_0 \sqrt{\epsilon_r \mu'}$, we get the spin-crossover angle as

$$\zeta_{sc} = \cos^{-1} \left(\sqrt{\frac{1}{\mu'}} \right). \quad (\text{D3})$$

- [1] W. Marynowski, R. Lech, and J. Mazur, *IEEE Trans. Microw. Theory Tech.* **65**, 4883 (2017).
- [2] K. Suzuki, *IEEE Trans. Electron Devices* **16**, 1018 (1969).
- [3] K. Suzuki and R. Hirota, *IEEE Trans. Electron Devices* **18**, 408 (1971).
- [4] M. Kanda and W. May, *IEEE Trans. Microw. Theory Tech.* **21**, 786 (1973).
- [5] G. N. Jawad, C. I. Duff, and R. Sloan, *IEEE Trans. Microw. Theory Tech.* **65**, 1249 (2017).
- [6] C. Valagiannopoulos, S. A. H. Gangaraj, and F. Monticone, *Nanomater. Nanotechnol.* **8**, 1847980418808087 (2018).
- [7] S. A. Hassani Gangaraj, C. Valagiannopoulos, and F. Monticone, *Phys. Rev. Res.* **2**, 023180 (2020).
- [8] D. M. Pozar, *Microwave Engineering*, 4th ed. (Wiley, New Delhi, India, 2012).
- [9] Z. Li and R.-x. Wu, *Appl. Phys. A* **124**, 139 (2018).
- [10] E. Arnaud, L. Huitema, R. Chantalat, A. Bellion, and T. Monediere, *Int. J. Microw. Wireless Technol.* **12**, 332 (2020).
- [11] A. Afshani and K. Wu, *IEEE Trans. Microw. Theory Tech.* **67**, 3350 (2019).
- [12] Y. Zhang, D. Cai, C. Zhao, M. Zhu, Y. Gao, Y. Chen, X. Liang, H. Chen, J. Wang, Y. Wei, Y. He, C. Dong, N. Sun, M. Zaeimbashi, Y. Yang, H. Zhu, B. Zhang, K. Huang, and N. X. Sun, *IEEE Trans. Microw. Theory Tech.* **68**, 5307 (2020).
- [13] B. Heinz, T. Brächer, M. Schneider, Q. Wang, B. Lägél, A. M. Friedel, D. Breitbach, S. Steinert, T. Meyer, M. Kewenig, C. Dubs, P. Pirro, and A. V. Chumak, *Nano Lett.* **20**, 4220 (2020).
- [14] V. Veerakumar and R. E. Camley, *Phys. Rev. B* **74**, 214401 (2006).
- [15] E. G. Lokk, *J. Commun. Technol. Electron.* **62**, 251 (2017).
- [16] Z. Zhou, J. Xin, X. Zhang, Y. Wang, and Y. Song, *Opt. Commun.* **423**, 145 (2018).
- [17] R. Macêdo, T. Dumelow, and R. L. Stamps, *ACS Photon.* **3**, 1670 (2016).
- [18] C. Lan, K. Bi, J. Zhou, and B. Li, *Appl. Phys. Lett.* **107**, 211112 (2015).
- [19] V. R. Tuz, *J. Magn. Magn. Mater.* **419**, 559 (2016).
- [20] V. R. Tuz and V. I. Fesenko, *J. Appl. Phys.* **128**, 013107 (2020).
- [21] V. I. Fesenko and V. R. Tuz, *Phys. Rev. B* **99**, 094404 (2019).
- [22] R. Yu, R. Alae, R. W. Boyd, and F. J. G. de Abajo, *Phys. Rev. Lett.* **125**, 037403 (2020).
- [23] H. N. S. Krishnamoorthy, Y. Zhou, S. Ramanathan, E. Narimanov, and V. M. Menon, *Appl. Phys. Lett.* **104**, 121101 (2014).
- [24] A. Poddubny, I. Iorsh, P. Belov, and Y. Kivshar, *Nat. Photon.* **7**, 948 (2013).
- [25] M. Durach, *Opt. Commun.* **476**, 126349 (2020).
- [26] P. Shekhar, J. Atkinson, and Z. Jacob, *Nano Convergence* **1**, 14 (2014).
- [27] X. Song, Z. Liu, Y. Xiang, and K. Aydin, *Opt. Express* **26**, 5469 (2018).
- [28] Z. Jacob, L. V. Alekseyev, and E. Narimanov, *Opt. Express* **14**, 8247 (2006).
- [29] A. Ghoshroy, W. Adams, X. Zhang, and D. O. Güney, *Opt. Lett.* **43**, 1810 (2018).
- [30] J. Shi, B. Liu, P. Li, L. Y. Ng, and S. Shen, *Nano Lett.* **15**, 1217 (2015).
- [31] F. Liu, L. Xiao, Y. Ye, M. Wang, K. Cui, X. Feng, W. Zhang, and Y. Huang, *Nat. Photon.* **11**, 289 (2017).
- [32] J. Tao, L. Wu, G. Zheng, and S. Yu, *Carbon* **150**, 136 (2019).
- [33] P. Shekhar, S. Pendharker, H. Sahasrabudhe, D. Vick, M. Malac, R. Rahman, and Z. Jacob, *Optica* **5**, 1590 (2018).
- [34] R. Macêdo and R. E. Camley, *Phys. Rev. B* **99**, 014437 (2019).
- [35] R.-C. Shiu, H.-C. Chan, H.-X. Wang, and G.-Y. Guo, *Phys. Rev. Mater.* **4**, 065202 (2020).
- [36] V. R. Tuz, I. V. Fedorin, and V. I. Fesenko, *Opt. Lett.* **42**, 4561 (2017).
- [37] M. Neugebauer, T. Bauer, A. Aiello, and P. Banzer, *Phys. Rev. Lett.* **114**, 063901 (2015).
- [38] A. Y. Bekshaev, K. Y. Bliokh, and F. Nori, *Phys. Rev. X* **5**, 011039 (2015).
- [39] J. Chen, C. Wan, L. J. Kong, and Q. Zhan, *Opt. Express* **25**, 19517 (2017).
- [40] M. Neugebauer, J. S. Eismann, T. Bauer, and P. Banzer, *Phys. Rev. X* **8**, 021042 (2018).
- [41] G. Rui, Y. Li, S. Zhou, Y. Wang, B. Gu, Y. Cui, and Q. Zhan, *Photon. Res.* **7**, 69 (2019).
- [42] K. Y. Bliokh and F. Nori, *Phys. Rev. A* **85**, 061801(R) (2012).
- [43] T. Van Mechelen and Z. Jacob, *Optica* **3**, 118 (2016).
- [44] K. Gotlieb, C.-Y. Lin, M. Serbyn, W. Zhang, C. L. Smallwood, C. Jozwiak, H. Eisaki, Z. Hussain, A. Vishwanath, and A. Lanzara, *Science* **362**, 1271 (2018).
- [45] S. Luo, L. He, and M. Li, *Nat. Commun.* **8**, 2141 (2017).
- [46] F. Kalhor, T. Thundat, and Z. Jacob, *Appl. Phys. Lett.* **108**, 061102 (2016).
- [47] H. Magallanes and E. Brasselet, *Nat. Photon.* **12**, 461 (2018).
- [48] V. Svak, O. Brzobohatý, M. Šiler, P. Ják, J. Kaňka, P. Zemánek, and S. H. Simpson, *Nat. Commun.* **9**, 5453 (2018).
- [49] S. Pendharker, F. Kalhor, T. V. Mechelen, S. Jahani, N. Nazemifard, T. Thundat, and Z. Jacob, *Opt. Express* **26**, 23898 (2018).
- [50] C. Triolo, A. Cacciola, S. Patanè, R. Saija, S. Savasta, and F. Nori, *ACS Photon.* **4**, 2242 (2017).